

Tailored focal beam shaping and its application in laser material processing

Cite as: J. Laser Appl. **31**, 042019 (2019);


Submitted: 04 August 2019 . Accepted: 21 October 2019 . Published Online: 14 November 2019

Anna Möhl, Sebastian Kaldun, Clemens Kunz , Frank A. Müller, Ulrike Fuchs , and Stephan Gräf 

COLLECTIONS

Paper published as part of the special topic on [Ultrafast Laser Technology 2019](#)

Note: This paper is part of the Special Collection: Ultrafast Laser Technology 2019.

 This paper was selected as Featured



View Online



Export Citation



CrossMark

ARTICLES YOU MAY BE INTERESTED IN

[Beam shaper increases femtosecond laser material processing speed and quality](#)

Scilight **2019**, 461110 (2019); <https://doi.org/10.1063/10.0000272>

[Picosecond laser lift-off method for fracture and debonding of copper oxide layer grown on copper substrate](#)

Journal of Laser Applications **31**, 042015 (2019); <https://doi.org/10.2351/1.5121339>

[Effects of laser beam lead angle on picosecond laser processing of silicon nitride ceramics](#)

Journal of Laser Applications **31**, 042011 (2019); <https://doi.org/10.2351/1.5126920>

ALIA



Tailored focal beam shaping and its application in laser material processing



Cite as: J. Laser Appl. 31, 042019 (2019); doi: 10.2351/1.5123051

Submitted: 4 August 2019 · Accepted: 21 October 2019 ·

Published Online: 14 November 2019



Anna Möhl,¹ Sebastian Kaldun,¹ Clemens Kunz,² Frank A. Müller,² Ulrike Fuchs,^{1,a)} and Stephan Cräf^{2,b)}

AFFILIATIONS

¹Asphericon GmbH, Stockholmer Str. 9, 07747 Jena, Germany

²Otto Schott Institute of Materials Research (OSIM), Friedrich Schiller University, Löbdergraben 32, 07743 Jena, Germany

Note: This paper is part of the Special Collection: Ultrafast Laser Technology 2019.

ABSTRACT

Besides the optimization of the laser and processing parameters, the adaptation of the focal intensity distribution offers great potential for a well-defined control of laser processing and for improving the processing results. In this paper, different tailored intensity distributions were discussed with respect to their suitability for femtosecond laser material processing on the micro- and nanoscale such as cutting, marking, and the generation of laser-induced periodic surface structures. It was shown by means of laser processing of stainless steel that the numerical simulations for the beam shaping unit are in good agreement with the experimental results. Also, the suitability of the beam shaping device to work with a scanner and an F-theta lens as commonly used for material processing was demonstrated. In this context, the improvement of the machining results was shown experimentally, and a significant reduction of the machining time was achieved.

Key words: femtosecond laser processing, beam shaping, donut, top-hat, laser-induced periodic surface structures

© 2019 Author(s). All article content, except where otherwise noted, is licensed under a Creative Commons Attribution (CC BY) license (<http://creativecommons.org/licenses/by/4.0/>). <https://doi.org/10.2351/1.5123051>

I. INTRODUCTION

The generation of tailored intensity distributions of the laser radiation in the focal region is still an active field of research with the aim of achieving a user-defined interaction with the material. For this purpose, the usually Gaussian laser radiation is converted into suitable beam profiles by means of special optics. In addition to increasing the efficiency of conventional laser processing such as cutting, drilling, and microablation, this transformation aims at reducing the achievable structural sizes and improving the quality of the processes mentioned above.^{1–3} Moreover, the beam shaping facilitates to create novel surface structures that are of potential interest, for example, for biomimetic surfaces with specific functional properties.^{4–6}

The beam shaping approaches are very diverse: In order to generate, e.g., top-hat profiles with a uniform intensity distribution over the beam cross section, apertures are used to select the flat portion from expanded Gaussian beams.⁷ Field mapping shapers enable to transform a Gaussian input beam into the desired field

distribution based on refractive^{8–10} and diffractive optical elements.^{7,11} Finally, beam integrators or homogenizers can be used to split the input beam into several beamlets that are superimposed in the output beam to ensure the homogeneous intensity distribution in a given working plane.^{7,12} As an alternative, spatial light modulators provide flexible optical devices that are able to dynamically modify the amplitude, phase, and polarization of an incoming laser beam and thus create versatile intensity profiles.^{13–15}

Refractive beam shapers are characterized, in particular, by their very high conversion efficiency and a simple structure. Compared to diffractive elements, they are easier to manufacture and more insensitive with respect to wavelength changes. Therefore, it is the subject of this work to introduce a very compact and flexible refractive, aspheric beam shaping element for material processing. In combination with a focusing lens, it transforms a collimated Gaussian intensity profile of the input beam into a focused beam with different focal intensity distributions including top-hat and donut profiles available in different working distances.

As an advantage, the modular system enables smooth integration into existing setups and the large input diameter of 10 mm allows the transformation of large radiation powers. Also, the beam shaper can be used with collimated laser beams or fiber-coupled sources. Furthermore, the input and output beams are scalable enabling a wide range of top-hat and donut widths provided by a single beam shaper.

A central aspect of this work was to clarify whether the device is suitable for material processing working with a scanner and an F-theta lens. This aspect is essential in order to optimally utilize the high repetition rates of modern laser systems and to ensure high processing efficiency. For this purpose, selected design investigations as well as results of the practical testing are presented. The latter was carried out on stainless steel as the substrate material using a Yb:KYW thin disc femtosecond laser (fs-laser). Application examples include surface nanostructuring based on laser-induced periodic surface structures (LIPSS), which are of great potential concerning functional surfaces,^{16,17} and surface microstructuring based on laser ablation as the conventional material processing technique.¹⁸ The formation and properties of LIPSS on stainless steel have been the subject of numerous studies.^{19–21} In general, the existence of different types of LIPSS was demonstrated by several authors. These structures can be generated in dependence on the laser and material parameters.^{17,22} The present study focuses on low-spatial frequency LIPSS on metals, hereinafter referred to as LIPSS. On metals, they are characterized by spatial periods Λ in the order of the utilized laser wavelength λ and an orientation perpendicular to the linear beam polarization.²²

II. GENERATING TAILORED FOCAL INTENSITY DISTRIBUTIONS

When talking about tailoring focal intensity distributions, one automatically enters the field of Fourier optics. Any lens used for focusing performs a Fourier transformation of the incoming intensity distribution into the focal plane. It is, therefore, a common approach to ask the inverse question of how the incoming beam profile needs to look like for a certain focal distribution.^{23,24} For homogenous surface structuring (e.g., based on LIPSS), the so-called top-hat distributions are very promising due to the uniform intensity distribution over the beam cross section.²⁵ Thus, to obtain a focused top-hat intensity distribution, the input intensity function needs to be the Fourier transform of a circ-function. Based on this knowledge, the optical design task comes down to a beam shaping that performs conversion of a collimated beam with a Gaussian intensity distribution to a collimated Bessel-sinc shaped profile. There are several ways to solve this. However, the most elegant way is to introduce a phase plate as described in Ref. 26. It overcomes the problem of generating the endless side maxima of the Bessel profile by simply assuming that the focal top-hat distribution does not need to have perfectly steep edges like a circ-function. The principle layout of this approach is shown in Fig. 1. As schematically depicted, the Bessel function is approximated by imitating the first root and the first side maximum only, skipping the higher spatial orders. This is done choosing the step height of the center region to introduce a phase delay of π within the $1/e^2$ diameter of the incoming Gaussian beam intensity distribution.

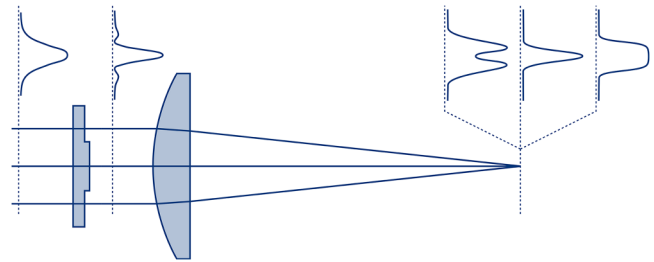


FIG. 1. Principle layout of the beam shaping system, consisting of a phase plate and a focusing optics, with the correlated intensity distributions in the focal region.

The working principle of this beam shaping system is based on manipulating the radial phase distribution of the incoming beam. Thus, it is changing the interference conditions in the whole focal region. Depending on the working distance, the focal intensity distribution changes significantly, which is illustrated in Fig. 2 by normalized beam profile sections along the propagation direction (z axis). The depicted range is ± 1.5 mm around the original waist position of the focusing lens ($f = 100$ mm, numerical aperture $NA = 0.05$ at 1025 nm) used. For better orientation, cross sections at five different working distances are shown, whereas the experimental results presented in Sec. IV are obtained at pos. 1–4. A closer examination of the focal region reveals the formation of three different top-hat profiles along the direction of propagation. The first two show slight fluctuations of the intensity at the top, and the last one (pos. 4) is the smoothest and most promising candidate for large-area LIPSS generation based on a scanning procedure.²⁵ The beam waist (pos. 3) is very similar to the beam waist generated by focusing without the phase plate. Its distance from the focusing lens is slightly increased. The donut profile (pos. 1) is highly interesting, too, as it changes the depth of the middle dip with the working distance. Thus, by choosing the working distance, the shape of this donut profile can be tuned. Another feature of this beam shaping approach is the scalability of the profile width with the NA of the focusing lens. Accordingly, a wider profile requires a lower NA. One way to achieve this would be to simply scale the focal length of the lens, but this leads to problems with the working distance as the focal length scales roughly linear with the profile width. For example, increasing the top-hat diameter from about 50 to $500\ \mu\text{m}$ can easily lead to an increase in focal length to 1 m or more when working with the same phase plate. Of course, it would also be possible to use different phase plates for different widths. We propose a modular combination that allows flexible and fast scaling with a minimum number of optical elements involved.

As for all beam shaping approaches, a specification of the incoming beam is needed as the resulting element will only work under this condition. For the practical realization of the beam shaping system, the input beam diameter ($1/e^2$) was defined as 10 mm on the left side of the phase plate also to ensure the feasibility for higher laser power. This automatically leads to the next question of how to adapt an arbitrary laser source to match this

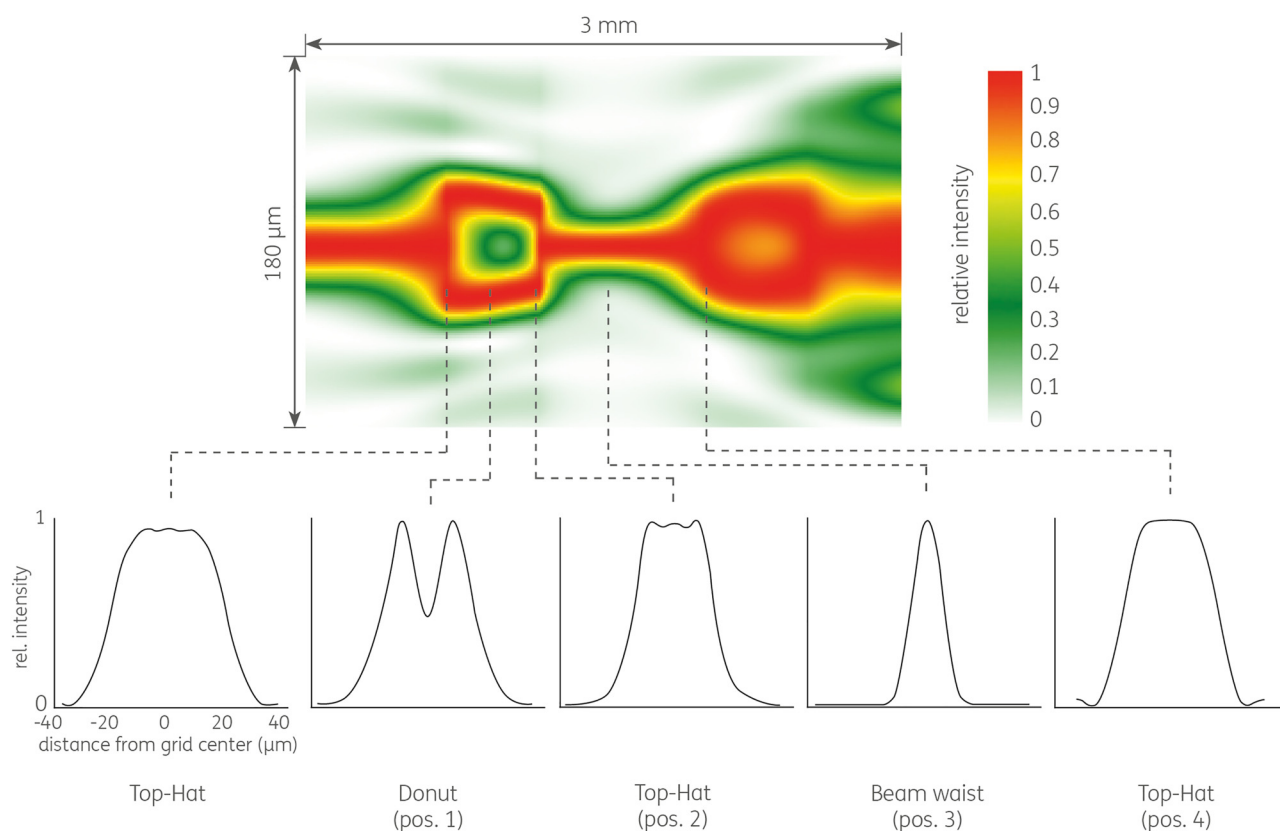


FIG. 2. Visualization of normalized beam profiles along the z -direction in a range of ± 1.5 mm around the focal plane and corresponding beam profiles for the different planes. Focusing lens has NA = 0.05 at 1025 nm with $f = 100$ mm. Positions pos. 1–4 correspond to the experimental results in Sec. IV.

input condition for the phase plate. This can be realized by beam expansion systems. If used together with the a|BeamExpanders, this is alignment free by just screwing all parts together due to the high precision mounts involved. In the case of a fiber-coupled laser source, an a|AspheriColl can be added.²⁷ Due to the chosen approach of generating a collimated Bessel-sinc-like profile, the system output is perfectly scalable by adding a|BeamExpanders behind the phase plate. This allows not only to generate nearly arbitrary dimensions of top-hat beam profiles but also to adapt the working distances. An exemplary layout of the discussed configuration is shown in Fig. 3.

For efficient material processing, it is essential to be able to use such a beam shaping unit with a (galvanometer) scanner system. The experimental results in Sec. IV were obtained with a maximum scan field of $(50 \times 50) \text{ mm}^2$. Therefore, Fig. 4 shows the numerical simulations of all relevant focal distributions (pos. 1–4) at the center, 5 mm (a tilt angle of 1.4°), 12.5 mm (a tilt angle of 3.5°), and 25 mm (a tilt angle of 7°) obtained with a perfect F-theta lens. These simulations show modifications, especially for the center dip/tip of the regions, for all profiles with increasing deflection angle. Partially this is caused by the perfect F-theta lens, which slightly changes the condition of Fourier transformation for each

deflection angle. Unfortunately, it was not possible to simulate the experimental setup with the real lens used. Nevertheless, the experimental results showed no such profile changes toward the edges of the scanning field.

III. MATERIALS AND METHODS

For laser material processing, a diode pumped Yb:KYW thin disk fs-laser system (JenLas D2.fs, Jenoptik, Germany) was used as the radiation source. The linearly polarized output beam was characterized by a central wavelength of $\lambda = 1025$ nm, a pulse duration of $\tau = 300$ fs (FWHM), a repetition frequency of $f_{\text{rep}} = 100$ kHz, and pulse energies $E_{\text{imp}} \leq 40 \mu\text{J}$. The Gaussian output beam ($M^2 \sim 1.08$) was widened by a beam expander (5 \times) and subsequently shaped by means of the beam shaping element (Fig. 5). Using a galvanometer scanner (IntelliScan14, Scanlab, Germany) equipped with an F-theta objective lens (JENar, Jenoptik, Germany) with a focal length of $f_L = 100$ mm, the laser beam was focused on the sample surface. The focal spot diameter in the beam waist (pos. 3 in Fig. 2) was experimentally determined to be $2w_f \sim 34 \mu\text{m}$ ($1/e^2$ -intensity) using the method proposed by Liu.²⁸ The focal intensity distributions along the z -direction were analyzed by a beam profiling camera (SP928, Ophir).

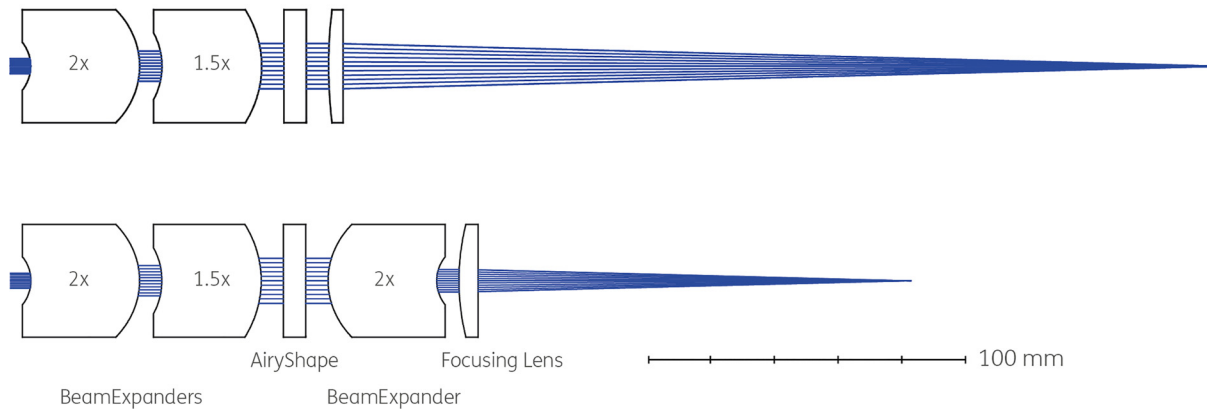


FIG. 3. Flexible adaption of input and output beam diameter of the beam shaping setup. Both configurations generate identical focal distributions, having the same NA as the shortening of the focal length ($f = 100$ mm) is compensated by scaling down the beam diameter by the same factor (bottom).

Commercially available austenitic stainless steel (X2CrNiMo17-12-2, Outokumpu, Germany) was used as the substrate material. The sample surface was manually grounded and polished to a mirror finish with an average surface roughness of $R_a \sim 4$ nm using SiC abrasive paper of 800, 1200, and 2400 grits and 6, 3, and $1\mu\text{m}$ polycrystalline diamond suspension, respectively. The laser processed sample surfaces were ultrasonically cleaned in acetone and isopropanol and subsequently characterized concerning their morphology by scanning electron microscopy (SEM) (SigmaVP, Carl Zeiss, Germany) at an accelerating voltage of 5 kV using a secondary electron detector. In this context, the

alignment and the spatial periods of the LIPSS were quantified by 2D-Fourier transform (2D-FT) analysis of the SEM micrographs. The surface topography was evaluated by white light interference microscopy (WLIM) (CCI HD, Taylor Hobson, Germany) equipped with a $50\times$ objective.

IV. RESULTS AND DISCUSSION

A. Single spot experiments

In a first step, the adequate function of the beam shaping element was evaluated by single spot experiments on stainless steel.

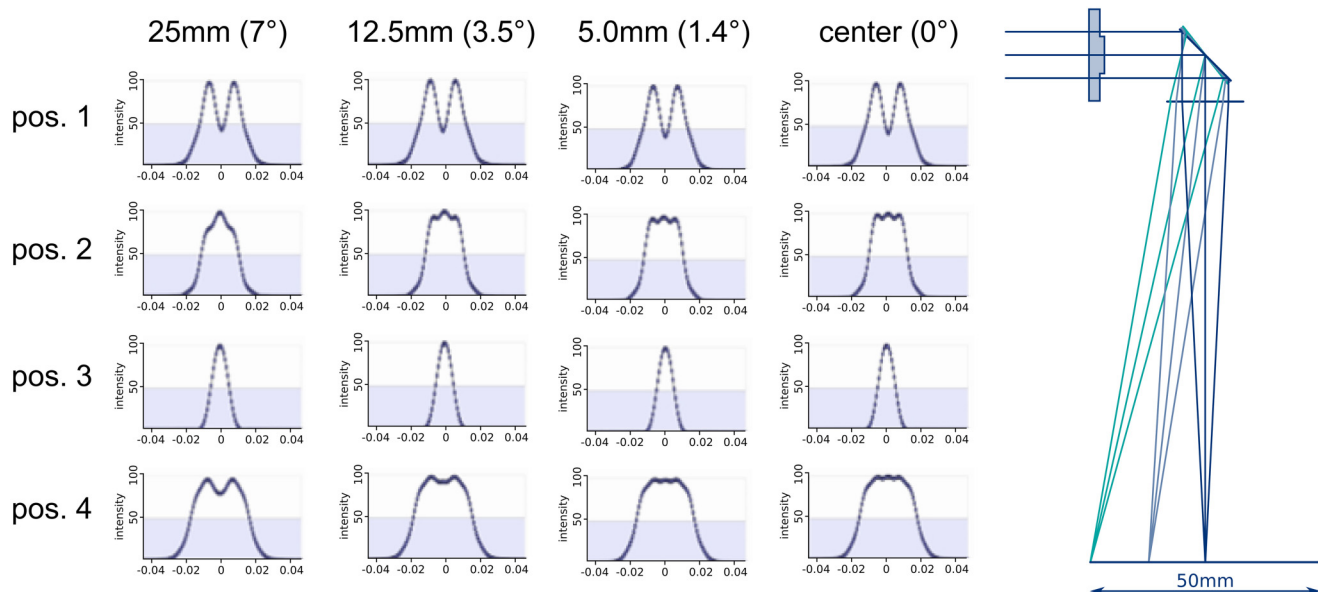


FIG. 4. Numerical simulations of all relevant focal distributions (pos. 1–4) at the center, 5 mm (tilt angle: 1.4°), 12.5 mm (tilt angle: 3.5°), and 25 mm (tilt angle: 7°) of the beam shaping unit when used with an ideal (galvanometer) scanner and a perfect F-theta lens. Positions pos. 1–4 correspond to the experimental results in Sec. IV.

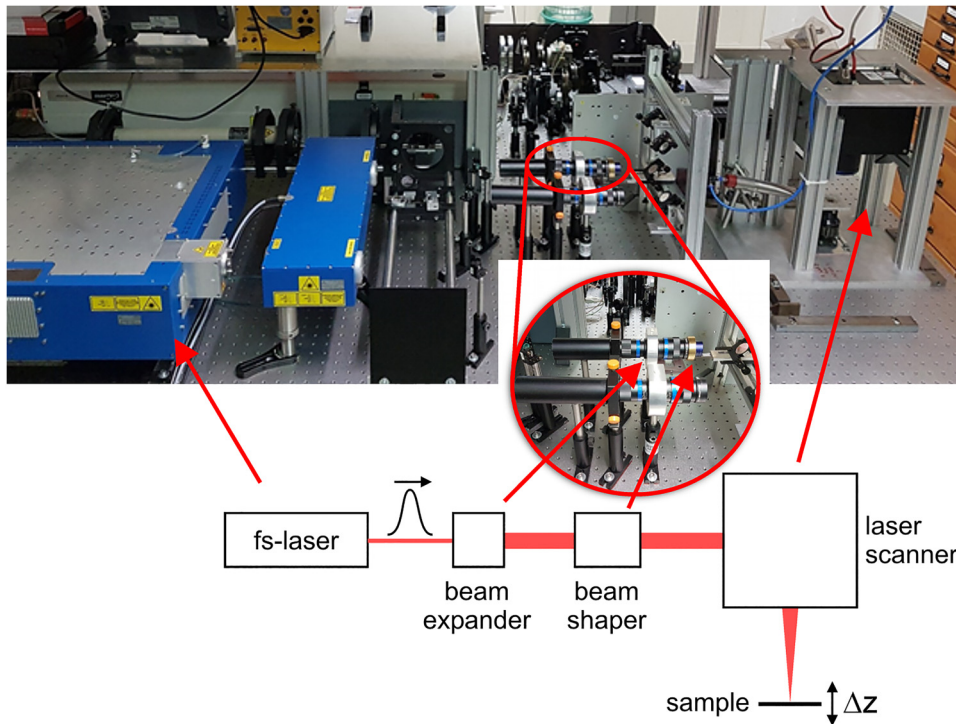


FIG. 5. Experimental setup used for the practical testing of the beam shaping element consisting of the fs-laser system, a beam expander (5×), the beam shaping element, and a galvanometer scanner equipped with an F-theta objective lens ($f_t = 100$ mm) for scanning the focused fs-laser beam over the sample surface.

For this purpose, the material surface was placed in the focal position under the focusing optics of the laser scanner, and the specific intensity profiles were selected based on the respective z -positions (Fig. 2). Figure 6 shows the corresponding SEM micrographs of the ablation spots obtained from irradiating the surface as a function of the fs-laser pulse number N . For all ablation spots, the surface was irradiated at normal incidence under an ambient air atmosphere, and the pulse energy E_{imp} was kept constant at $13 \mu\text{J}$. The latter results in a variation of the fs-laser peak fluence F due to the deviating diameters of the beam profiles (Fig. 2). In the Gaussian beam waist (pos. 3) with the smallest beam diameter of $2w_f \sim 34 \mu\text{m}$, the utilized pulse energy results in an fs-laser peak fluence of $F = 2E_{\text{imp}}/(\pi w_f^2) = 2.8 \text{ J/cm}^2$. The comparison of the SEM micrographs reveals the ability to generate tailored focal intensity distributions at the sample surface in dependence of the z -position. The depth of the corresponding ablation craters increases with increasing N . The donut-shaped intensity profile (pos. 1) leads to a ring-shaped ablation geometry provided by the well-pronounced minimum of intensity in the center of the beam profile [Figs. 6(a)–6(c)]. In this area, the material surface remains unaffected by the laser radiation even at the highest pulse number $N = 200$. The ablation spot fabricated with the top-hat profile (pos. 2) exhibits a slightly modulated surface topography [Figs. 6(d)–6(f)]. In the beam waist (pos. 3), the SEM micrographs reveal melt formation [Figs. 6(g) and 6(h)] and an excessive, inhomogeneous ablation in the center of the ablation crater, which can be observed, in particular, for the largest pulse number of $N = 200$ [Fig. 6(i)]. Both effects are caused by the very high

intensity in the center of the Gaussian beam profile accompanied by heat accumulation effects. On the contrary, the unmodulated, flat plateau of the top-hat intensity profile (pos. 4) results in a very homogeneous ablation over the beam cross section [Figs. 6(j)–6(l)].

A detailed analysis of Fig. 6 reveals the appearance of characteristic nanostructures in the ablation spots induced by fs-laser irradiation. They refer to LIPSS that are characterized by a spatial period of about 940 nm (i.e., $\Lambda \sim 0.9 \cdot \lambda$). In accordance with the literature of LIPSS formation on metals, they exhibit an orientation perpendicular to the linear polarization as indicated by the direction of the electrical field vector E in Fig. 6(j).^{19,20,22} These experimental observations on metals support the well-accepted theory that describes the formation of LIPSS by interference effects of incident light with electromagnetic waves scattered at the rough material surface.²⁹ Alternative approaches to explain their formation include self-organization of the irradiated material resulting from laser-induced thermodynamic instabilities that lead to the redistribution of the material.^{30,31} The single spot experiments reveal that the LIPSS orientation is independent of the focal intensity distribution. Similar results were reported using radial, azimuthal, and spiral structures generated by cylindrical vector fs-laser beams.^{4–6} Moreover, significant differences concerning the periodicity of the LIPSS fabricated with the different intensity distributions were not observed. This aspect is consistent with other studies that demonstrated only a minor influence of the fs-laser peak fluence F on the spatial period in the fluence ranges where LIPSS is experimentally obtained.^{5,32} It is worth mentioning that, in the intensive center of

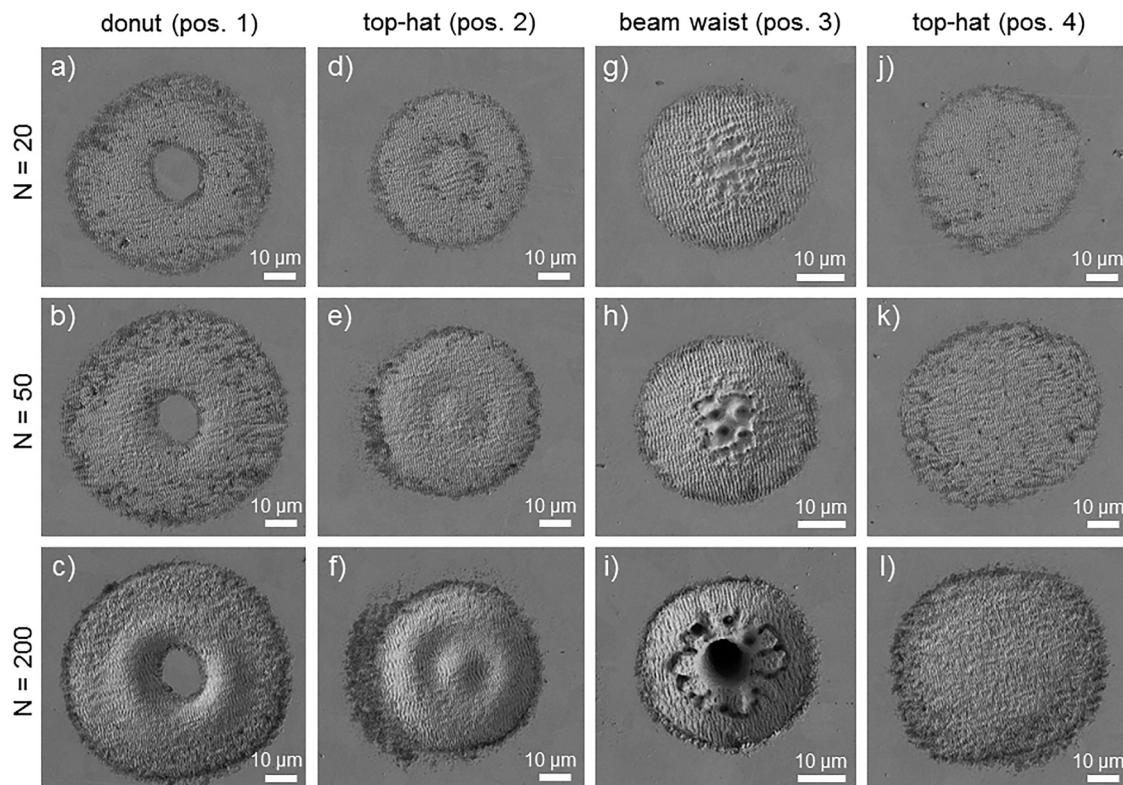


FIG. 6. SEM micrographs of the stainless steel surface upon irradiation with the specific beam profiles provided by the beam shaping element at the different z-positions as a function of the laser pulse number N . In all experiments, the pulse energy E_{imp} was kept constant at $13 \mu\text{J}$. The direction of the electrical field vector E of the linearly polarized radiation is indicated in (j).

the beam, waist LIPSS is superimposed by melt formation, which led to larger structural features such as microholes. In contrast, a well-pronounced LIPSS pattern was generated homogeneously over the entire ablation spot by means of the top-hat profile (pos. 4).

Figure 7 illustrates the comparison of SEM micrographs and WLIM micrographs obtained from the ablation spots ($N=200$) with the intensity distributions measured with the beam profiling camera. The results demonstrate a very good agreement between theoretical and experimental results. This concerns on the one hand the correlation of geometric aspects such as beam and ablation diameters and on the other hand the agreement of characteristic features of the respective intensity distributions with the resulting surface topography. The latter is particularly emphasized by the donut-shaped beam profile [Fig. 7(a)] as well as by the slight modulation of the surface topography related to the top-hat profile (pos. 2) [Fig. 7(b)]. With regard to the geometric aspects, ablation diameters of about $70 \mu\text{m}$ (pos. 1), $53 \mu\text{m}$ (pos. 2), $35 \mu\text{m}$ (pos. 3), and $62 \mu\text{m}$ (pos. 4) were determined by WLIM, which are in the order of magnitude of the simulated beam diameters. In addition, a value of about $20 \mu\text{m}$ was measured for the ablation depth in the beam waist, which is almost twice as large as for the other beam profiles. This can be explained by the distribution of the constant

pulse energy to the larger beam diameters, which results in a reduced fs-laser peak fluence.

B. Large-area structuring with LIPSS

Functional surfaces based on LIPSS for industrial applications require in most cases the ability to produce large surface areas with high quality at reasonable costs. In addition to the homogeneity of the structures, the processing time plays an important role in this context. Figure 8(a) shows an LIPSS pattern that was produced by unidirectional scanning of the surface using a scanning velocity of $v = 0.67 \text{ m/s}$, a lateral spacing of $\Delta x = 6 \mu\text{m}$ between two adjacent scan lines, a pulse energy of $E_{\text{imp}} = 2.6 \mu\text{J}$, and the Gaussian beam profile in the beam waist. The corresponding focal spot diameter $2w_f = 34 \mu\text{m}$ is indicated by the circle in the SEM micrograph. It becomes evident that the generated gratinglike structures consist of highly regular LIPSS oriented perpendicular to the linear polarization. The micrograph reveals that LIPSS can be coherently written over a large area despite the linewise scanning process. The properties of the grating with respect to the spatial period, orientation, and homogeneity can be quantitatively described by 2D-FT of the SEM micrograph [inset in Fig. 8(a)]. The cross section

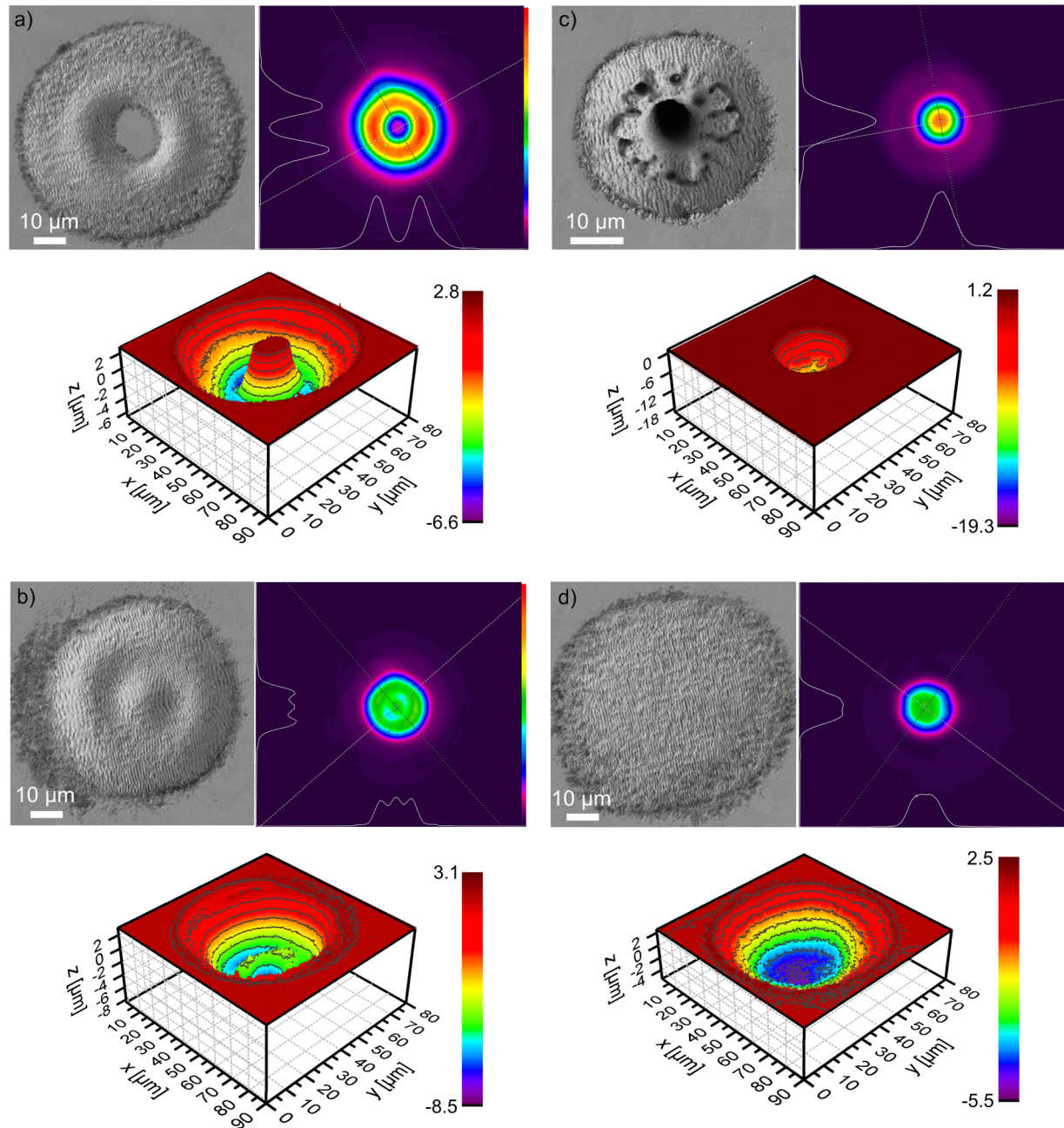


FIG. 7. Comparison of the calculated focal intensity distributions with SEM micrographs and WLIM micrographs of the ablation spots fabricated with $N = 200$, $E_{\text{imp}} = 13 \mu\text{J}$, and the corresponding intensity profiles: (a) donut (pos. 1), (b) top-hat (pos. 2), (c) Gaussian beam waist (pos. 3), and (d) top-hat (pos. 4). Note the different scaling of the color bars in the WLIM micrographs, which indicate the determined ablation depth in micrometers.

demonstrates in terms of the narrow characteristic peak that the spatial period is limited to a very narrow range. It was determined to be $(940 \pm 30) \text{ nm}$. Based on the method described by Gnilytskyi *et al.*,²¹ the dispersion of the LIPSS orientation angle was

determined to be $\delta\theta \sim 9^\circ$. This small value confirms the perfect alignment of the gratinglike structures. For completeness, typical values of the modulation depth of the LIPSS pattern are in the order of 200 nm.^{19,20} In order to achieve large areas of well-

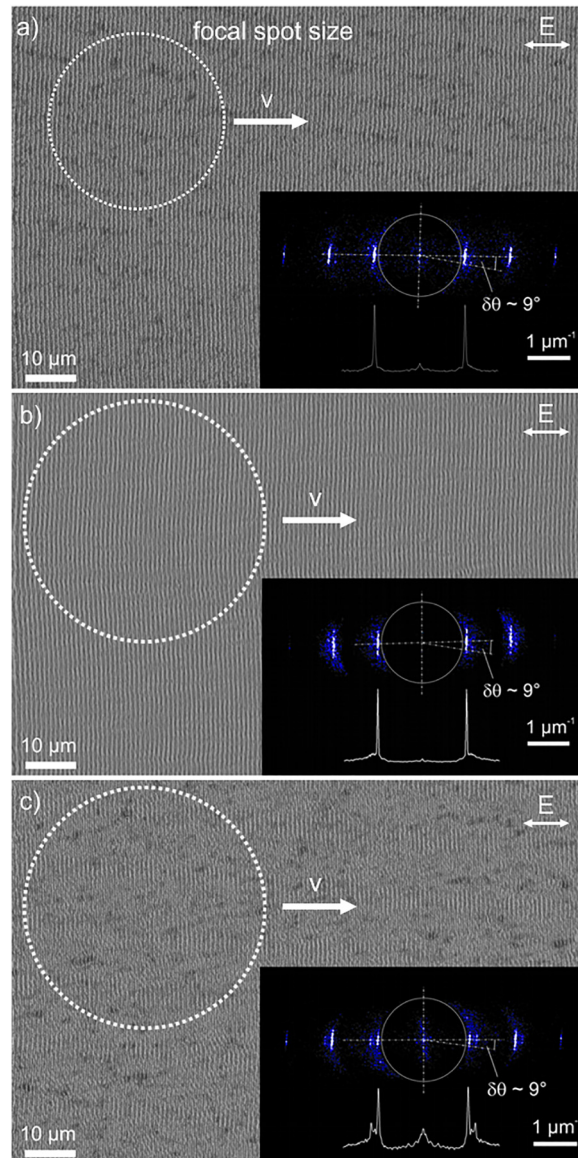


FIG. 8. SEM micrographs of the stainless-steel surface structured with LIPSS using linearly polarized fs-laser radiation: (a) Gaussian beam profile ($2w_f \sim 34 \mu\text{m}$, $E_{\text{imp}} = 2.6 \mu\text{J}$, $v = 0.67 \text{ m/s}$, and $\Delta x = 6 \mu\text{m}$), (b) top-hat ($2w_f \sim 47 \mu\text{m}$, $E_{\text{imp}} = 6 \mu\text{J}$, $v = 0.67 \text{ m/s}$, and $\Delta x = 6 \mu\text{m}$), and (c) top-hat ($2w_f \sim 47 \mu\text{m}$, $E_{\text{imp}} = 6 \mu\text{J}$, $v = 1.2 \text{ m/s}$, and $\Delta x = 6 \mu\text{m}$). The respective beam diameters are illustrated by the white dotted circles. The insets correspond to the 2D-FT of the SEM micrographs and their corresponding cross sections, which quantify the homogeneity and orientation of the LIPSS. Here, $\delta\theta$ refers to the dispersion of the LIPSS orientation angle, and the laser wavelength ($0.975 \mu\text{m}^{-1}$) is indicated by the white circle in the 2D-FT spectra.

pronounced LIPSS with the top-hat profile (pos. 4) as well, the pulse energy was increased to $E_{\text{imp}} = 6 \mu\text{J}$ [Fig. 8(b)]. The SEM micrograph and its Fourier transformation confirm a similar quality of the fabricated LIPSS pattern in terms of spatial period

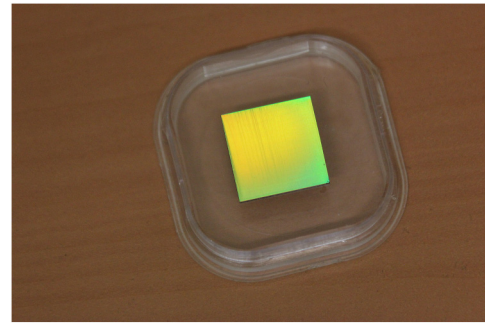


FIG. 9. Structural colors on a stainless steel sample of $(10 \times 10) \text{ mm}^2$ obtained from white light illumination. The corresponding LIPSS pattern illustrated in Fig. 8(c) was fabricated with the focal top-hat intensity profile (pos. 4).

and alignment. The most striking feature of LIPSS-based surfaces is related to the appearance of varying colors observed at different viewing angles upon illumination with white light.^{33–35} They originate from the diffraction behavior of the gratinglike structures. Figure 9 illustrates these structural colors on the stainless steel surface structured with a top-hat focal intensity distribution [Fig. 8(c)]. For the top-hat profile (pos. 4), the SEM micrograph in Fig. 8(c) demonstrates that the scanning velocity can be doubled to $v = 1.2 \text{ m/s}$ without further optimization of the processing parameters. The calculated Fourier transformation shows that the quality of the surface pattern remained almost constant. The resulting reduction of the processing time by a factor of 2 (approx. 30 s per cm^2), however, results in a significant advantage for the economic scaling of the structuring process to large surface areas.

C. Conventional material processing

Figure 10 shows SEM micrographs obtained from channel-like structures fabricated by fs-laser ablation on stainless steel as a function of the number of overscans. The channels were prepared with the same parameters ($v = 0.1 \text{ m/s}$, $E_{\text{imp}} = 11.3 \mu\text{J}$) in order to allow direct comparability of the topography induced by the different focal intensity distributions. All SEM micrographs obtained from the surface after a single overscan illustrate once again the possibility to coherently write LIPSS by means of a scanning process [Figs. 10(a), 10(e), and 10(i)]. With an increase in the number of overscans, the ablation depth generally increases, resulting in microscale channel-like structures, whose surface is superimposed with the nanoscale LIPSS. In this context, it becomes evident that, due to the smallest beam diameter in the beam waist, the narrowest channel with a width of about $30 \mu\text{m}$ and a depth of about $20 \mu\text{m}$ can be generated. Analogous to the single spot experiments, the bottom of the channel in Fig. 10(f) is characterized by an inhomogeneous ablation after several overscans, which results from the high intensity in the beam center. The other two beam profiles result in larger channel widths and smaller ablation depths and exhibit a very homogeneous ablation. This is also confirmed by the WLIM micrographs in Figs. 10(d), 10(h), and 10(l) that illustrate the 3D geometry of the corresponding channels obtained from ten

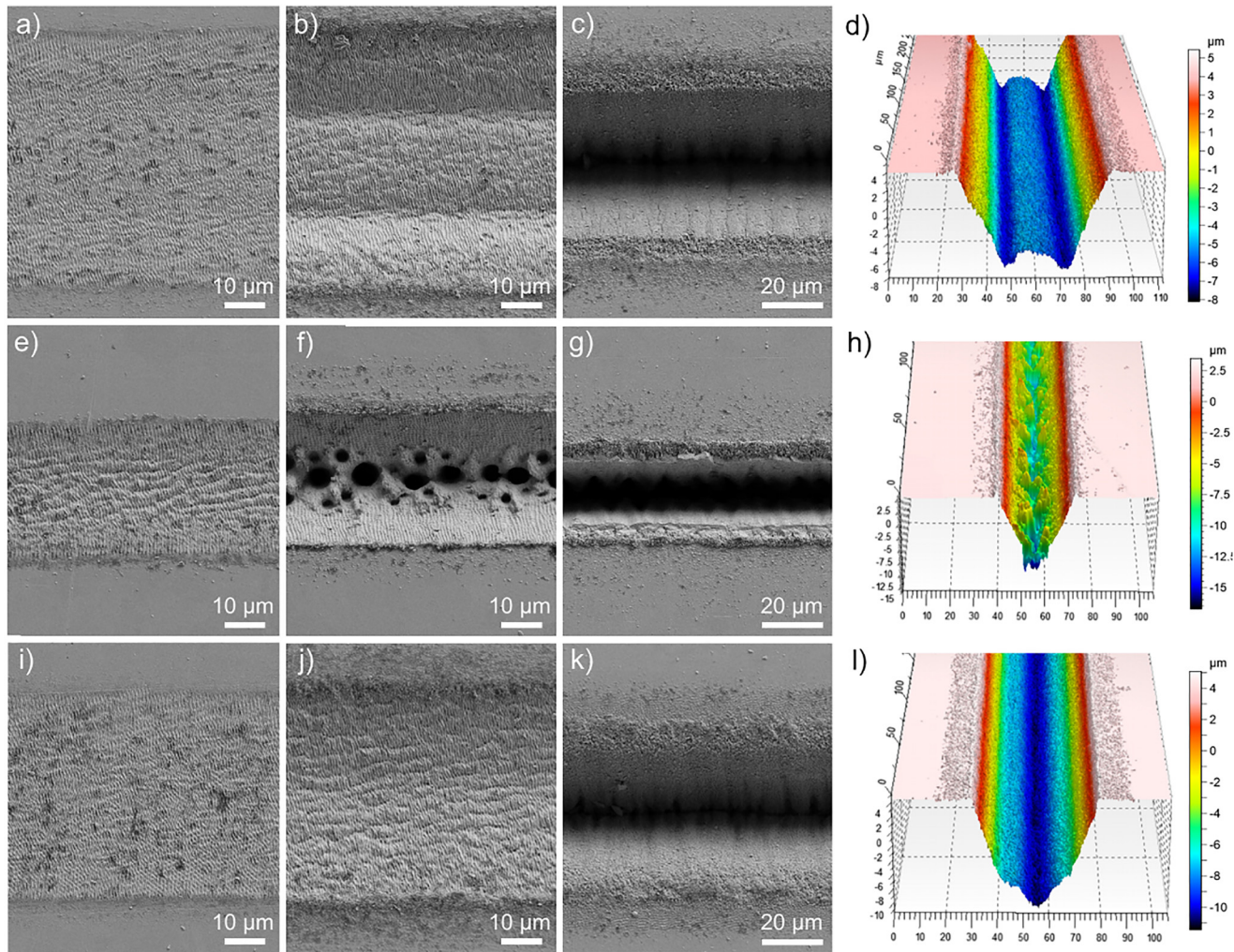


FIG. 10. SEM micrographs of channel-like structures fabricated by fs-laser ablation on stainless steel with $v=0.1$ m/s and $E_{\text{imp}}=11.3$ μJ as a function of the number of overscans using different focal intensity distributions: (a)–(c) donut (pos. 1), (e)–(g) Gaussian beam waist, and (i)–(l) top-hat (pos. 4). WLM micrographs in (d), (h), and (l) illustrate the 3D geometry of the corresponding channels obtained from ten overscans.

overscans. The micrographs reveal that at this stage of processing the respective beam profile is reflected in the cross section of the channels. Consequently, the beam shaping element, in particular, by means of donut and top-hat profiles, facilitates to realize specific wall inclination angles as well as tailor-made cross-sectional geometries of the channels in a relatively simple way by changing the z -position of the sample surface. Additionally, the spot size can be utilized to scale the width of those geometries, as discussed in Sec. II.

V. CONCLUSIONS

In this paper, various tailored intensity distributions are discussed with respect to their suitability for material processing on

the micro- and nanoscale such as cutting, material ablation, and the fabrication of LIPSS. Numerical simulations for the beam shaping unit predicted the generation of several different intensity distributions, which could all be experimentally verified by beam profiling and laser processing. More specifically, there are three different top-hat profiles generated in the focal region, of which one (pos. 4) was used to generate very homogeneous large-area LIPSS. Furthermore, the processing speed was doubled by using the beam shaping unit when compared to the conventional approach of focusing a Gaussian beam. Thus, it was possible to structure a surface area of 1 cm^2 within approx. 30 s. Additionally, the focused top-hat profile and a donut profile are compared to a focused Gaussian beam by creating channel-like structures via multiple line scans, which is typical for microstructuring of materials. The utilization of

these other focal intensity distributions results in precise channels with well-defined walls and without melt artifacts as observed with the conventional approach. Thus, we propose using such tailored focal distributions for deterministic micromachining.

REFERENCES

- ¹M. Malinauskas, A. Zukauskas, S. Hasegawa, Y. Hayasaki, V. Mizeikis, R. Buividas, and S. Juodkazis, "Ultrafast laser processing of materials: From science to industry," *Light Sci. Appl.* **5**, e16133 (2016).
- ²K. Sugioka and Y. Cheng, "A tutorial on optics for ultrafast laser materials processing: Basic microprocessing system to beam shaping and advanced focusing methods," *Adv. Opt. Technol.* **1**, 353–364 (2012).
- ³G. Raciukaitis, E. Stankevicius, P. Gecys, M. Gedvilas, C. Bischoff, E. Jager, U. Umhofer, and F. Volklein, "Laser processing by using diffractive optical laser beam shaping technique," *J. Laser Micro Nanoeng.* **6**, 37–43 (2011).
- ⁴O. J. Allegre, W. Perrie, S. P. Edwardson, G. Dearden, and K. G. Watkins, "Laser microprocessing of steel with radially and azimuthally polarized femtosecond vortex pulses," *J. Opt.* **14**, 085601 (2012).
- ⁵E. Skoulas, A. Manousaki, C. Fotakis, and E. Stratakis, "Biomimetic surface structuring using cylindrical vector femtosecond laser beams," *Sci. Rep.* **7**, 45114 (2017).
- ⁶J. Ouyang, W. Perrie, O. J. Allegre, T. Heil, Y. Jin, E. Fearon, D. Eckford, S. P. Edwardson, and G. Dearden, "Tailored optical vector fields for ultrashort-pulse laser induced complex surface plasmon structuring," *Opt. Express* **23**, 12562–12572 (2015).
- ⁷F. M. Dickey, "Theory and techniques for laser beam shaping," in *International Congress on Applications of Lasers & Electro-Optics Jacksonville, Florida, October 2001* (The Laser Institute, Orlando, FL, 2001), pp. 1393–1402.
- ⁸B. R. Frieden, "Lossless conversion of a plane laser wave to a plane wave of uniform irradiance," *Appl. Opt.* **4**, 1400–1403 (1965).
- ⁹P. W. Rhodes and D. L. Shealy, "Refractive optical systems for irradiance redistribution of collimated radiation—Their design and analysis," *Appl. Opt.* **19**, 3545–3553 (1980).
- ¹⁰J. A. Hoffnagle and C. M. Jefferson, "Design and performance of a refractive optical system that converts a Gaussian to a flattop beam," *Appl. Opt.* **39**, 5488–5499 (2000).
- ¹¹W. B. Veldkamp and C. J. Kastner, "Beam profile shaping for laser radars that use detector arrays," *Appl. Opt.* **21**, 345–356 (1982).
- ¹²S. Bollanti, P. Di Lazzaro, and D. Murra, "More about the light beam shaping by the integration method," *Eur. Phys. J. Appl. Phys.* **28**, 179–186 (2004).
- ¹³T. Häfner, J. Strauss, C. Roeder, J. Heberle, and M. Schmidt, "Tailored laser beam shaping for efficient and accurate microstructuring," *Appl. Phys. A* **124**, 111 (2018).
- ¹⁴J. Li, Z. Kuanga, J. G. Vilara, G. Deardena, W. Perrie, and S. Edwardson, "Dynamic ultrafast laser beam shaping for material processing at the imaging plane using a spatial light modulator," paper presented at the 9th International Conference on Photonic Technologies LANE, Fürth, Germany, September 19–22, 2016.
- ¹⁵Y. Jin, O. J. Allegre, W. Perrie, K. Abrams, J. Ouyang, E. Fearon, S. P. Edwardson, and G. Dearden, "Dynamic modulation of spatially structured polarization fields for real-time control of ultrafast laser-material interactions," *Opt. Express* **21**, 25333–25343 (2013).
- ¹⁶F. Müller, C. Kunz, and S. Gräf, "Bio-inspired functional surfaces based on laser-induced periodic surface structures," *Materials* **9**, 476 (2016).
- ¹⁷J. Bonse, S. Höhm, S. V. Kirner, A. Rosenfeld, and J. Krüger, "Laser-induced periodic surface structures—A scientific evergreen," *IEEE J. Sel. Top. Quant.* **23**, 9000615 (2017).
- ¹⁸K. Sugioka, M. Meunier, and A. Piqué, *Laser Precision Microfabrication* (Springer, Berlin, 2010).
- ¹⁹S. Gräf and F. A. Müller, "Polarisation-dependent generation of fs-laser induced periodic surface structures," *Appl. Surf. Sci.* **331**, 150–155 (2015).
- ²⁰S. Gräf, C. Kunz, A. Undisz, R. Wonneberger, M. Rettenmayr, and F. A. Müller, "Mechano-responsive colour change of laser-induced periodic surface structures," *Appl. Surf. Sci.* **471**, 645–651 (2019).
- ²¹I. Gnilitzky, T. J. Y. Derrien, Y. Levy, N. M. Bulgakova, T. Mocek, and L. Orazi, "High-speed manufacturing of highly regular femtosecond laser-induced periodic surface structures: Physical origin of regularity," *Sci. Rep.* **7**, 8485 (2017).
- ²²J. Bonse, J. Krüger, S. Höhm, and A. Rosenfeld, "Femtosecond laser-induced periodic surface structures," *J. Laser. Appl.* **24**, 042006 (2012).
- ²³J. W. Goodman, *Introduction to Fourier Optics*, 3rd ed. (Roberts, Englewood, Co, 2005).
- ²⁴F. M. Dickey, *Laser Beam Shaping: Theory and Techniques*, 2nd ed. (CRC, Boca Raton, FL, 2014).
- ²⁵S. Schwarz, S. Rung, C. Esen, and R. Hellmann, "Homogeneous low spatial frequency LIPSS on dielectric materials generated by beam-shaped femtosecond pulsed laser irradiation," *J. Laser Micro Nanoeng.* **13**, 90–94 (2018).
- ²⁶J. Cordingley, "Method for severing integrated-circuit connection paths by a phase-plate-adjusted laser beam," U.S. patent 5,300,756 (October 22, 1991).
- ²⁷A. Möhl and U. Fuchs, "Exploring the unlimited possibilities of modular aspheric Gauss to top-hat beam shaping," *Adv. Opt. Technol.* **5**, 201–210 (2016).
- ²⁸J. M. Liu, "Simple technique for measurements of pulsed Gaussian beam spot sizes," *Opt. Lett.* **7**, 196–198 (1982).
- ²⁹J. E. Sipe, J. F. Young, J. S. Preston, and H. M. van Driel, "Laser-induced periodic surface structure. I. Theory," *Phys. Rev. B* **27**, 1141–1154 (1983).
- ³⁰P. Gregoric, M. Sedlacek, B. Podgornik, and J. Reif, "Formation of laser-induced periodic surface structures (LIPSS) on tool steel by multiple picosecond laser pulses of different polarizations," *Appl. Surf. Sci.* **387**, 698–706 (2016).
- ³¹J. Reif, F. Costache, and M. Bestehorn, "Self-organized surface nanostructuring by femtosecond laser processing," in *Recent Advances in Laser Processing of Materials*, edited by J. Perriere, E. Millon, and E. Fogarassy (Elsevier, New York, 2006), pp. 275.
- ³²C. A. Zuhlke, G. D. Tsibidis, T. Anderson, E. Stratakis, G. Gogos, and D. R. Alexander, "Investigation of femtosecond laser induced ripple formation on copper for varying incident angle," *APL Adv.* **8**, 015212 (2018).
- ³³B. Dusser, Z. Sagan, H. Soder, N. Faure, J. P. Colombier, M. Jourlin, and E. Audouard, "Controlled nanostructures formation by ultra fast laser pulses for color marking," *Opt. Express* **18**, 2913–2924 (2010).
- ³⁴G. Q. Li, J. W. Li, Y. L. Hu, C. C. Zhang, X. H. Li, J. R. Chu, and W. H. Huang, "Femtosecond laser color marking stainless steel surface with different wavelengths," *Appl. Phys. A* **118**, 1189–1196 (2015).
- ³⁵A. Y. Vorobyev and C. Guo, "Colorizing metals with femtosecond laser pulses," *Appl. Phys. Lett.* **92**, 041914 (2008).



海纳光学

电话: 0755-84870203
网址: www.highlightoptics.com